

Directly Grown Universally Doped Ultrathin Nanocrystalline Carbon Overlayer Sustains Pragmatic Zinc Metal Anodes

Xianzhong Yang

Soochow University

Jiaze Lv

Soochow University

Cai Cheng

Sichuan Normal University

Zixiong Shi

Soochow University

Jun Peng

Universität Hamburg

Ziyan Chen

Soochow University

Xueyu Lian

Soochow University

Weiping Li

Soochow University

Yuhan Zou

Soochow University

Yu Zhao

Soochow University

Mark H. Rümmeli

Soochow University

Shixue Dou

University of Wollongong

Jingyu Sun (✉ sunjy86@suda.edu.cn)

Soochow University

Research Article

Keywords:

Posted Date: May 18th, 2022

DOI: <https://doi.org/10.21203/rs.3.rs-1667853/v1>

License:  This work is licensed under a Creative Commons Attribution 4.0 International License.

[Read Full License](#)

Abstract

Rechargeable Zn-ion battery has emerged as a promising alternative to Li-ion battery owing to the high safety and environmental benignity. Nevertheless, dendritic formation and side reaction occurred at the anode side greatly handicap its practical advance. Here, we put forward an effective maneuver to sustain practical Zn anode by optimizing the anode/electrolyte interface, which deals with the direct growth of an ultrathin nitrogen and oxygen co-doped carbon (NOC) overlayer over Zn foil *via* a scalable plasma enhanced chemical vapor deposition. Thus-designed NOC overlayer can guide the stable Zn deposition along Zn (002) because of the favorable adsorption by dopant atoms and cultivation effect of nanocrystalline carbons, thereby inducing a planar Zn texture. Moreover, the abundant heteroatoms help reduce the solvation energy and accelerate the reaction kinetics. As a result, dendrite growth and side reaction are concurrently mitigated. Symmetric cell harvests durable electrochemical cycling (1125 h at $10.0 \text{ mA cm}^{-2}/1.0 \text{ mAh cm}^{-2}$; 136 h at $30.0 \text{ mA cm}^{-2}/30.0 \text{ mAh cm}^{-2}$). Assembled full battery further realizes elongated lifespans under stringent conditions. This strategy marks a new avenue for the *in-situ* construction of ultrathin protective coating to optimize the Zn deposition electrochemistry toward pragmatic Zn anode.

One Sentence Summary

The directly grown N/O co-doped nanocrystalline carbon film on commercial Zn foil enables uniform Zn deposition by guiding preferential growth along Zn (002) plane, holding promise for the practicability of aqueous Zn-ion batteries.

Introduction

Aqueous batteries have emerged as appealing candidates for grid-scale energy storage due to the overwhelming advantages of low cost and high safety, amongst which the rechargeable aqueous Zn-ion battery (AZIB) has stimulated a burgeoning interest to implement mass production and practical application (1–3). Thereinto, Zn metal harnesses a low redox potential (-0.762 V vs. standard hydrogen electrode) and a high theoretical capacity (820 mAh g^{-1} , 5855 mAh cm^{-3}), making it a desirable anode material in pursuit of high-energy battery system (4–6). Nonetheless, the major obstacles compromising durable Zn anode lie in uncontrollable dendrite growth, adverse hydrogen evolution reaction, and detrimental by-product formation (7, 8). In further contexts, the potential practicability of Zn anode is plagued by the inferior electrochemical stability especially under the heavy-duty operations of large current density and high Zn utilization (9, 10).

The robust anode/electrolyte interface is a key prerequisite for realizing highly reversible Zn anodes (4, 11). To date, a myriad of interface engineering strategies has been explored with an emphasis on tailoring artificial solid electrolyte interface (SEI) (12, 13). Nevertheless, most of SEI layers derived from traditional coating routes are prone to possess considerable thickness (*i.e.*, $> 10 \text{ }\mu\text{m}$), which might jeopardize the overall energy density of the entire AZIB. Because of their light-weighted feature, structural

diversity and tunable doping level, carbonaceous materials are promising candidates to build artificial SEI (5, 14–17). Along this line, chemical vapor deposition (CVD) strategy, which allows the direct growth of ultrathin graphene on various substrates, is anticipated to enable the conformal graphitic formation on Zn surface and afford negligible volume/mass contribution. However, suffering from the low melting point of Zn metal, such a route involving thermal treatment has not yet done the trick in the realm of Zn anode protection.

Considering that the Zn metal anode cycles through hostless Zn^{2+}/Zn stripping/plating, the crystallographic texture of deposited Zn is critical to the morphology and reversibility of Zn (18). In this sense, decoding the crystallite geometry and orientational order plays a vital role in digging deep into the complicated Zn electrodeposition process (19). Despite fruitful achievements (14, 15, 17), Zn deposition electrochemistry mediated by carbonaceous SEI architectures remains elusive by far. Related investigations on Zn nucleation and growth mechanism are rather lacking from the crystallographic perspective. Even worse, most of the reported Zn anodes modified by carbonaceous materials can rarely operate under an elevated current density ($> 5 \text{ mA cm}^{-2}$) to meet the ever-increasing demand for fast-charging. Equally importantly, they are also difficult to maintain a longevous cyclic operation under high Zn utilization conditions (9) (depth of discharge, DOD $> 40\%$), substantially impeding the commercialization of Zn anodes. Therefore, it is essential and imperative to introduce an ultrathin carbonaceous SEI to cultivate textured crystal plane toward stabilized Zn anodes operating at large current density and high Zn utilization.

Here, we develop a scalable plasma-enhanced chemical vapor deposition (PECVD) strategy to realize the direct growth of ultrathin N/O co-doped nanocrystalline carbon (NOC) overlayer on Zn metals. The thickness of the directly grown NOC overlayer can be tuned to *ca.* 20 nm, far thinner as compared with those formed *via* other prevailing routes. The presence of N and O dopants and the hexagonal nanocrystalline could guide the stable formation of Zn (002) but distorted change of Zn (100) and (101), which is in favor of tailoring dendrite-free Zn deposition along the preferable (002) plane. Meanwhile, the NOC overlayer enables enhanced adsorption of water molecules in solvated Zn^{2+} and hence facilitates the desolvation process. Thanks to the *in-situ* interface modulation, symmetric cell with NOC@Zn anode can sustain a durable operation at stringent conditions of $30.0 \text{ mA cm}^{-2}/30.0 \text{ mAh cm}^{-2}$ and $20.0 \text{ mA cm}^{-2}/36.0 \text{ mAh cm}^{-2}$. More encouragingly, assembled full cells comprising NOC@Zn anode and vanadium oxide cathode demonstrate a prolonged lifespan under high current density, low negative-to-positive capacity ratio (N/P ratio) and bending conditions.

Results

Synthesis and characterization of NOC overlayer

With the consideration of the low melting point of Zn ($419.5 \text{ }^\circ\text{C}$), a PECVD route (20) was devised to *in-situ* grow ultrathin NOC overlayer directly on commercial Zn foil at a temperature range of $300 - 400 \text{ }^\circ\text{C}$.

As depicted in Fig. 1A, pyridine was used as the precursor to ensure the generation of N-containing carbon species under plasma treatment. The carrier gas Ar (containing a trace amount of O₂) can aid the transport of carbon species from upstream to Zn metal surface (21, 22). Impressively, the color of Zn foil rapidly turns to light brown upon reaction for 10 min, implying the successful formation of carbon coating (fig. S1). During the growth, nitrogen and oxygen atoms are simultaneously incorporated into the carbon skeleton (23, 24). The thickness of carbon overlayer could be adjusted by the growth time, which is simply reflected by the varied color of coated Zn surface (Fig. 1B). More impressively, a macroscopically sized sample with a lateral dimension of 20 cm × 12 cm can be obtained by employing a 4-inch furnace (Fig. 1C), holding promise for the scalable production of NOC@Zn materials in an economic fashion.

Raman spectra of NOC overlayers produced at different reaction temperatures were collected (fig. S2), where two peaks centering at 1345 and 1596 cm⁻¹ are attributed to the typical D band (defective feature) and G band (graphitic feature) signals of carbonaceous materials, respectively. The D/G intensity ratio (I_D/I_G) gradually decreases from 0.98 to 0.93 with the rise of growth temperature from 300 to 380°C, indicative of improved crystallinity (25). The disappearance of X-ray diffraction (XRD) signals of graphite might be owing to the poor crystallinity (fig. S3). X-ray photoelectron spectroscopy (XPS) measurement was carried out to probe the chemical composition of as-grown NOC film (fig. S4). The survey spectrum bears out the existence of Zn, C, N, and O elements. The C 1s spectrum encompasses four peaks at 284.4, 285.2, 286.1, and 287.8 eV, which can be respectively assigned to sp^2 C = C, sp^2 C = N, sp^3 C–N, and C–OH bonding (23). In addition, N 1s spectrum can be deconvoluted into the signals of pyridinic-N (N_{py} , 398.5 eV), pyrrolic-N (N_{pr} , 400.1 eV), and graphitic-N (N_{gr} , 401.7 eV) (20, 26), disclosing the abundant N dopants in NOC overlayer.

Representative scanning electron microscopy (SEM) observation of thus-produced NOC@Zn demonstrates a film-like morphology with a wealth of randomly distributed cracks (Fig. 1D and fig. S5A, B), which might originate from the uneven thermal distribution during the PECVD reaction. The thickness of Zn foil decreases by ~ 4 μm (from 10 to 6 μm) upon PECVD process because of the thermal sublimation effect (fig. S5C, D). Atomic force microscopy (AFM) inspections indicate that the thickness of NOC overlayer can be tailored at *ca.* 20 nm after 10 min synthesis (Inset of Fig. 1D and fig. S6). Transmission electron microscopy (TEM) characterizations further corroborate the lamellar feature of NOC overlayer (Fig. 1E and fig. S7A). The diffraction ring can be recognized in the selected area electron diffraction (SAED) patterns (Inset of Fig. 1E), implying the formation of graphitic nanodomains (27) in NOC overlayer. This is evidenced by the atomically resolved TEM imaging to show nano-sized honeycomb lattice of graphene (Fig. 1F and fig. S7B-D). Energy dispersive X-ray spectroscopy (EDS) mapping under high-angle annular dark field-scanning TEM (HAADF-STEM) mode in Fig. 1G showcases the homogeneous distribution of C, N, and O elements. These results collectively verify the successful preparation of NOC overlayer affording N/O co-doping over Zn foil by PECVD. Furthermore, upon the introduction of heteroatom dopants in NOC overlayer, the electrolyte contact angle decreases from 87° to

61° (fig. S8). It is anticipated that the enhanced wettability is beneficial to facilitating the ion transport and hence reversible Zn plating/stripping (28).

Electrochemical performance of NOC@Zn

Cyclic voltammetry (CV) curves of Ti–Zn half cells were collected to probe the Zn electrodeposition behavior in the presence of NOC overlayer. As shown in Fig. 2A, the apparently lower Zn nucleation overpotential on NOC@Ti than that on bare Ti is beneficial to activating more nucleation sites, thereby promoting uniform Zn deposition. Note that the NOC@Ti–Zn cell maintains a steady cycling over 400 cycles under 2.0 mA cm⁻²/0.5 mAh cm⁻² (Fig. 2B and fig. S9), whereas the bare Ti–Zn cell can merely sustain up to 100 cycles with a drastic fluctuation of Coulombic efficiency (CE) values. More encouragingly, the NOC@Ti–Zn cell can obtain an average CE of 99.5% over 800 cycles under an elevated current density of 10.0 mA cm⁻² (Fig. 2C and fig. S10), which is superior to its counterpart. The voltage hysteresis of NOC@Ti–Zn cell is far lower than that of bare Ti–Zn cell.

Symmetric cell measurements were carried out to further elucidate the reversibility of Zn plating/stripping under the regulation of NOC overlayer. As shown in Fig. 2D, the NOC@Zn symmetric cell acquires a stable cycling performance over 1125 h with a low voltage hysteresis at 10.0 mA cm⁻²/1.0 mAh cm⁻², whose cyclic life is approximately ten times longer than bare Zn symmetric cell. As such, the voltage hysteresis of bare Zn cell increases gradually and ultimately augments to an irreversible value, implying the rapid cell failure without the protection of NOC overlayer. In comparison, the voltage hysteresis of NOC@Zn can maintain at 60 mV upon cycling for 1125 h, indicative of the effective inhibition of dendrite growth and by-product formation (29). Note that an optimized NOC thickness of 20 nm could be gained in response to enabling a prolonged cycle life with a small polarization (fig. S11). The NOC@Zn symmetric cell further displays durable cycling performances with low voltage hysteresis at 5.0 mA cm⁻²/5.0 mAh cm⁻² and 10.0 mA cm⁻²/10.0 mAh cm⁻² (fig. S12). Remarkably, it can still sustain a stable cycling operation over 136 h under 30.0 mA cm⁻²/30.0 mAh cm⁻² (Fig. 2E and fig. S13A), outperforming most of the state-of-the-art Zn electrodes under such a stringent condition.

Since the prevailing Zn metal anodes are typically compromised by shallow DOD (10), it is meaningful to augment the Zn utilization to evaluate the protective effect of NOC overlayer. In this sense, the NOC@Zn symmetric cell enables a stable cycling over 60 h under a plating/stripping capacity of 36.0 mAh cm⁻² (Fig. 2F and fig. S13B). Note that the corresponding DOD reaches ~ 64%, which is far higher as compared to most reported Zn anodes (table S1, 2). In addition, the NOC@Zn symmetric cell harvests a lower voltage hysteresis than bare Zn symmetric cell at each current density varying from 1.0 to 40.0 mA cm⁻² (fig. S13C), implying facile charge transfer kinetics under the management of NOC overlayer. To acquire a comprehensive understanding of electrochemical performance, the calculated cumulative capacity of NOC@Zn symmetric cell can be substantially elevated to 1080, 1800, 2200, and even 5625 mAh cm⁻² under different working conditions (Fig. 2G), which is superior to that of bare Zn symmetric cell.

Obviously, the NOC overlayer can boost homogeneous Zn nucleation and growth toward highly reversible dendrite-free Zn anode.

Mechanistic insight into the protection effect of NOC overlayer

To shed light on the protective mechanism of NOC overlayer, exhaustive characterizations in combination with electrochemical measurements were carried out. *Operando* optical microscopy was first employed to visualize Zn plating behavior with a current density of 5.0 mA cm^{-2} (fig. S14). After electrodeposition for 10 min, a multitude of protrusions randomly appear on the surface of bare Zn, which becomes increasingly obvious during electrodeposition (Fig. 3A and video S1). NOC@Zn electrode otherwise maintains a smooth surface morphology without discernible dendrites (Fig. 3B and video S2). The detailed morphologies of Zn plating were disclosed by SEM to further elucidate the impact of NOC overlayer on mitigating the dendrite. As depicted in Fig. 3C and fig. S15A, Zn flakes with high dip angles are randomly deposited on bare Zn, whilst hexagonal Zn plates on NOC@Zn are parallel to the substrate and exhibit a highly ordered orientation (Fig. 3D and fig. S15B). Upon plating/stripping for 100 cycles at $10.0 \text{ mA cm}^{-2}/1.0 \text{ mAh cm}^{-2}$, rampant dendrites and pits can be observed on the surface of bare Zn foil (Fig. 3E and fig. S15C). In stark contrast, the NOC@Zn electrode enables a dense and flat Zn deposition morphology (Fig. 3F and fig. S15D). Optical surface profilometry imaging further shows the NOC@Zn electrode displays a far smaller surface height difference ($6 \mu\text{m}$, Fig. 3H) as compared to the bare Zn ($50 \mu\text{m}$, Fig. 3G) after electrochemical cycling, in good agreement with side-view SEM observation (fig. S15E, F). Consequently, the NOC overlayer can facilitate the homogeneous Zn deposition and suppress the dendrite growth even under high current densities (fig. S16).

XRD was employed to investigate the crystal structure of electrodes after Zn deposition. The (002) intensity on NOC@Zn is greatly enhanced in comparison with bare Zn (Fig. 3I), implying a highly oriented deposition. The guided (002)-oriented Zn deposition *via* NOC overlayer contributes to a dendrite-free morphology of NOC@Zn anode. With respect to the bare Zn electrode, a noticeable peak at 8.6° can be recognized in the XRD pattern, which is ascribed to the formation of detrimental by-product $(\text{Zn}_4\text{SO}_4(\text{OH})_6 \cdot 4\text{H}_2\text{O})$ (4). Nonetheless, this diffraction peak can scarcely be observed for NOC@Zn electrode, suggesting that side reactions can be effectively mitigated by the NOC overlayer. In addition, the NOC@Zn symmetric cell possesses a higher transference number (30) than bare Zn (Fig. 3J and fig. S17), implying that the NOC overlayer can promote Zn^{2+} transport and hence facilitate homogenous Zn deposition.

The orientation of deposited Zn plates plays a vital role in influencing the electric field distribution of Zn anode. In this case, finite element simulation based on COMSOL Multiphysics was carried out to explore the electric field distributions (fig. S18). With respect to the bare Zn, the electrical field at the corner of vertical plates is drastically enhanced (Fig. 3K), which would accordingly trigger uneven Zn deposition. On the contrary, the horizontal Zn plates endow the NOC@Zn electrode with homogeneously distributed electrical field (Fig. 3L). These results uncover that the horizontal deposition of Zn plates can aid to

homogenize the electric field distribution, thereby further contributing to a uniform ion flux and ultimately promoting the reversibility of Zn anode (16).

The planar Zn deposition morphology is of paramount significance to the construction of highly durable NOC@Zn anode. To demystify its origin, density functional theory (DFT) calculations were performed with the aim to reveal the adsorption mechanism of N and O atoms on different crystal planes including Zn (002), Zn (100) and Zn (101) (Fig. 4A, B, and fig. S19). This is anticipated to further help exploring the role of NOC overlayer in manipulating Zn nucleation. Note that the free N/O atoms and fully relaxed crystal surface were selected as initial sites for structural optimization. Our DFT calculation indicates that the adsorption energy of N/O atom on Zn (002) is slightly lower than that on Zn (100) and Zn (101) (table S3), which might originate from the higher stability of Zn (002) facet (18, 31). More intriguingly, the optimized adsorption configurations imply that the N/O atom is prone to bury into the Zn (100) or Zn (101) surface, in contrast to the adsorption scenario on Zn (002). Consequently, the moderate binding energy of N/O atom on Zn (002) is beneficial to guiding preferential nucleation along Zn (002) plane at the initial stage of electrodeposition. However, the unstable embedded configurations manifest that the Zn nuclei can barely grow along Zn (100) and Zn (101) during plating process. In other words, the incorporated N/O atoms in the carbon skeleton could induce the nucleation along Zn (002).

Note further that the NOC layer possesses a poor electrical conductivity of $\sim 3.0 \times 10^{-6} \text{ S cm}^{-1}$ (fig. S20), which prevents the reduction and deposition of Zn on its forefront surface. In this sense, Zn^{2+} need to pass through the NOC layer to reach the surface of Zn metal, at which they will be reduced to Zn^0 . Fortunately, the NOC layer harnessing local interplanar spacing of 3.4 Å and abundant vacancies/defects can offer feasible diffusion paths for Zn^{2+} with a radius of 0.75 Å. As reported (32), the small mismatch (7%) of hexagonal lattice between graphene and Zn (002) plane can guarantee a heteroepitaxial deposition behavior. Therefore, the graphitic nanocrystal domain affording hexagonal lattice decorated in the NOC layer can effectively cultivate the preferential growth along Zn (002), which is in line with reported ZnSe overlayer (4). Collectively, the NOC overlayer promotes Zn (002)-dominated nucleation and growth behaviors, thereby mitigating the dendrite formation and ensuring the excellent stability of Zn plating/stripping process.

Apart from mass transfer, the solvation sheath of Zn^{2+} ($\text{Zn}(\text{H}_2\text{O})_6^{2+}$) is also a key to regulating the interfacial redox reaction (33, 34). It is well established that Zn^{2+} can be reduced and deposited on the electrode only after removing the solvation sheath (35). To elucidate the effect of NOC layer on modulating the solvation structure in charge-transfer process, the adsorption energy between H_2O and NOC layer was accordingly calculated. Note that the optimized adsorption configurations of H_2O with five adsorption sites are depicted (Fig. 4C and fig. S21). The relatively low binding energy (-0.14 eV) between pristine graphene and H_2O molecule would give rise to a weak adsorption effect (Fig. 4D). With the incorporation of O doping ($-\text{OH}$), the binding energy increases to -0.34 eV , indicative of an enhanced capture capability for H_2O . With respect to the three types of N doping, the pyrrolic N harvests the highest

binding energy of -0.39 eV. These simulation results suggest that $\text{Zn}(\text{H}_2\text{O})_6^{2+}$ is prone to interact with NOC overlayer with the aid of pyrrolic N and $-\text{OH}$ sites, thereby facilitating the desolvation process.

The electrochemical impedance spectra (EIS) at varied temperatures were collected to unravel the desolvation effect of NOC overlayer. It is evident that the charge-transfer resistance (R_{ct} , table S4) is drastically reduced with the assistance of NOC layer (Fig. 4E and fig. S22). As illustrated in Fig. 4F, the quantitatively derived activation energy (4, 36) (E_a) of NOC@Zn symmetric cell (21.3 kJ mol^{-1}) is considerably lower than that of bare Zn (46.3 kJ mol^{-1}), manifesting that the NOC overlayer can promote redox kinetics at the electrode/electrolyte interface by facilitating desolvation process. The high ionic conductivity of the NOC layer is beneficial to its Zn^{2+} transport (fig. S23). The Zn^{2+} diffusion dynamics tested by chronoamperometry imply the introduction of NOC layer can effectively inhibit the two-dimensional diffusion (36), thereby promoting homogeneous deposition (fig. S24). The linear polarization test was carried out to explore the corrosion of Zn anode (Fig. 4G). In comparison with the bare Zn anode, the corrosion potential of NOC@Zn obtains a positive shift (from -0.956 V to -0.950 V). In addition, the declined corrosion current by $\sim 302.3 \mu\text{A cm}^{-2}$ also suggests the effective restriction of corrosion effect with the presence of NOC overlayer. Therefore, the NOC overlayer avoids the direct contact between Zn anode and electrolyte, which further inhibits the side reaction and corrosion effect (16).

Taken together, the plating and cycling process on bare Zn and NOC@Zn anodes are schematically illustrated (Fig. 4H, I). In the case of bare Zn anode, a wealth of randomly distributed Zn plates, pits and H_2 bubbles aggregate on the surface after repeated plating/stripping, thereby resulting in a curtailed lifespan. In contrast, the NOC overlayer can mitigate dendrite growth and stabilize Zn anode *via* two mechanisms. For one thing, it can guide the oriented nucleation of hexagonal Zn plates and enable the in-parallel deposition with respect to the substrate. For another, it can significantly boost the interfacial redox kinetics by decreasing desolvation energy, thus ultimately achieving a prolonged cycle life.

AZIB full cell performance

To envisage the potential usage of NOC@Zn anode in practical devices, AZIB full cells comprising a $\text{KV}_{12}\text{O}_{30-y}\cdot n\text{H}_2\text{O}$ (KVOH) (4, 37) cathode and a NOC@Zn anode were assembled. The NOC@Zn - KVOH cell delivers an initial capacity of 149 mAh g^{-1} and maintains at 137 mAh g^{-1} after 4000 cycles at 10.0 A g^{-1} (Fig. 5A). In stark contrast, the bare Zn - KVOH cell undergoes a rapid capacity decay due to the rampant dendrite growth and side reactions (35, 38). Rate performance measurements indicate that NOC@Zn - KVOH cell harvests an advanced capacity at each current density as compared to bare Zn - KVOH, especially at the high rates (Fig. 5B). Such an excellent rate capability could be attributed to the robust anode/electrolyte interface. Nyquist plots reveal that the NOC@Zn - KVOH cell exhibits lower charge-transfer resistance and faster ion diffusion kinetics in comparison with the bare Zn-KVOH counterpart (fig. S25).

As a matter of fact, low loading cathodes ($\sim 1.0 \text{ mg cm}^{-2}$) and thick Zn anodes ($\geq 100 \text{ }\mu\text{m}$) were ubiquitously employed in previously reported AZIB systems (3, 32). Consequently, the N/P ratio is typically higher than 50, which greatly hinders the improvement of energy density. It is imperative and meaningful to increase the mass loading of cathodes and reduce the thickness of Zn anodes. To corroborate the outstanding electrochemical performance of the as-prepared NOC@Zn anodes in AZIB full cells, high-loading cathodes (5.59 mg cm^{-2}) and thin Zn foils ($10 \text{ }\mu\text{m}$) were employed. As aforementioned, the inevitable sublimation of Zn occurs in the PECVD process and hence the thickness of Zn foil can be decreased from $10 \text{ }\mu\text{m}$ to $6 \text{ }\mu\text{m}$, which stands for a capacity of 3.51 mAh cm^{-2} . Shown in Fig. 5C, the cyclic durability degrades in response to the reduction of N/P ratio. Encouragingly, the NOC@Zn - KVOH cell can sustain a stable operation over 400 cycles at 5.0 A g^{-1} at a low N/P ratio of 3.5. Figure 5D draws a comparison of current density and areal capacity based on Zn anode between this work and previous reports (table S5) (4, 8, 35, 39–46), manifesting the superiority of NOC@Zn anode in potential fast-charging scenarios.

More impressively, NOC@Zn anode harnessing mechanical robustness enables facile construction of bendable full cells in pursuit of flexible energy storage applications (fig. S26). As depicted in Fig. 5E, KVOH cathode and NOC@Zn anode are separated by glass fiber and encapsulated by polyimide tape (47). Two full cells in series can easily power a light-emitting diode (LED) indicator (Fig. 5F) or an electronic timer (Fig. 5G), showcasing the promising application potentials. Benefiting from its mechanical robustness, such a full cell harvesting a low charge-transfer resistance (fig. S27) delivers stable operation over 250 cycles under different bending states (Fig. 5H). Notably, the bendable full cell achieves a high capacity retention of 68% with a bending angle of 90° . These evaluations collectively substantiate that the NOC overlayer can inhibit parasitic reactions at the anode/electrolyte interface and guide uniform Zn deposition, ultimately in favor of elevating the stability and durability of practical AZIB.

Discussion

High-performance NOC@Zn anode has been developed through directly growth of N/O co-doped nanocrystalline carbon on commercial Zn foil utilizing a PECVD method. The ultrathin NOC layer can not only enable dendrite-free deposition by guiding preferential growth along Zn (002) plane, but also accelerate the kinetics of Zn^{2+} deposition via reducing desolvation energy, thereby mitigating H_2 evolution and side reactions. As a result, symmetric cell based on NOC@Zn electrodes demonstrates a low voltage hysteresis and outstanding cyclic stability at all testing current densities/capacities, even under harsh conditions ($30.0 \text{ mA cm}^{-2}/30.0 \text{ mAh cm}^{-2}$; $20.0 \text{ mA cm}^{-2}/36.0 \text{ mAh cm}^{-2}$). A cumulative capacity as high as 5625 mAh cm^{-2} can be achieved when cycled at 10.0 mA cm^{-2} , representing one of the advanced performances. More encouragingly, full batteries equipped with NOC@Zn anodes deliver remarkable cycling stability under high rate, low N/P ratio and bending conditions. Our NOC@Zn anodes affording versatility and simplicity may greatly promote the commercialization of Zn-ion batteries.

Materials And Methods

Synthesis of NOC@Zn

NOC@Zn was synthesized throughout a direct PECVD route. The pure Zn foil (thickness: 100 or 10 μm) was thoroughly cleaned with ethanol and water in order to remove impurities prior to use. The substrate was subsequently placed at the center of the furnace. The CVD system was pumped with a base pressure of 2 Pa and purged with a mixed carrier gas consisting of 0.2 standard cubic centimeters per minute (sccm) O_2 and 20 sccm Ar. Upon reaching to 380 $^\circ\text{C}$ within 5 min, the plasma (80 W) was turned on to allow the growth of 10 min with pyridine as precursor. After the PECVD reaction, the furnace was cooled down to room temperature under Ar.

Preparation of KVOH cathodes

The cathode (4) were fabricated by mixing active material (KVOH), conductive carbon (Super P) and polyvinylidene fluoride (PVDF) binder with a mass ratio of 7:2:1. The as-prepared slurry was uniformly dispersed in N-Methyl-2-Pyrrolidone (NMP) solvent, which was dropped onto Ti foil. The thus-fabricated electrodes were dried in a vacuum oven under 80 $^\circ\text{C}$ for 12 h to remove the residual solvent. The mass loading of active materials is 1.0~5.6 mg cm^{-2} .

Characterization

The morphologies of prepared samples were inspected by SEM (Hitachi, SU-8010). The as-grown NOC film was firstly transferred on copper mesh using a polymer-assisted transfer technology (48). Then the detailed structure, selected area electron diffraction and elemental maps of samples were recorded on TEM (FEI, Titan Themis Cubed G2 300; 80–300 kV). The confocal Raman spectrometer (LabRAM HR Evolution) was used to acquire the Raman spectra. To analyze the surface chemistry of samples, XPS measurements were carried out by the Escalab 250Xi Spectrophotometer. XRD patterns were collected on the Bruker D8 Advance Diffractometer. The contact angle was measured using Contact Angle System SL200KS (Solon Tech. (Shanghai) Inc., China). The optical surface profilometry images were captured on Leica DCM8 microsystems.

Electrochemical tests

Three types of CR2032 coin cells were assembled to investigate the electrochemical performances, including Zn–Zn symmetric cell, Ti–Zn asymmetric cell, and Zn–KVOH full cell. As-prepared electrodes were cut into circle discs. The cells were assembled with the commercial glass fiber as separator (WhatmanTM) and 2 M ZnSO_4 as electrolyte. Current–time curves and EIS were collected on CHI660E electrochemical workstation CHI660E. galvanostatic charge/discharge, rate, and cycling measurements were performed on the Neware battery-testing instrument. The linear-sweep voltammograms (LSVs) were recorded with a potential ranging from -1.15 to -0.75 V (vs. Ag/AgCl) at a scan rate of 5 mV s^{-1} .

Theoretical calculations

The geometry optimization and adsorption energy of N/O atoms are obtained based on first-principles plane wave calculations within density functional theory as implemented in the Vienna ab-initio simulation package (VASP) (49-51). The projector augmented-wave method (52) and Perdew-Burke-Ernzerhof exchange-correlation functional (53) are used. A cutoff energy of 400 eV for the plane-wave basis set and a Monkhorst-Pack mesh (54) of $4 \times 4 \times 1$ for the Brillouin zone integration are employed for Zn (002), Zn (100) and Zn (101) slabs relaxation and self-consistent calculations. Zn (002), Zn (100) and Zn (101) slabs with periodically repeating (4×4) unit cell by 5 layers was constructed for the N/O atom adsorption. The lower two layers of atoms are fixed to maintain the same with bulk structure. The thickness of vacuum layer was set to 17 Å. For H₂O adsorption, the Monkhorst-Pack mesh of $5 \times 1 \times 1$ for the Brillouin zone integration is employed for N-graphene ribbon relaxation and self-consistent calculations. All the structures are fully relaxed by conjugate gradient method until the maximum Hellmann-Feynman force acting on each atom is less than 0.01 eV/Å. In our calculation, the Grimme's D3 dispersion correction method is used (55). The adsorption energy was calculated by the formula: $E_{\text{ads}} = E_{\text{total}} - E_{\text{slab}} - E_{\text{Zn}}$, where E_{total} , E_{slab} and E_{Zn} are the total energy with/without the adsorption of Zn atom and atomic energy of Zn, respectively.

Electric field simulation

Finite element analysis conducted by COMSOL Multiphysics software was adapted to compare the electric field distribution at the interface between Zn hexagonal plates on the electrode and electrolyte. According to the two distinguished states of Zn hexagonal plates in the SEM images, two simplified three-dimensional models were established. In the models, one cuboid (8 μm length × 8 μm width × 7 μm height) represents the 2 M ZnSO₄ electrolyte with conductivity of 5 S m⁻¹, and the other cuboid (8 μm length × 8 μm width × 1 μm height) below the electrolyte represents Zn electrode. Regular hexagon sheets with different sizes were used to present the Zn hexagonal sheets produced during the charge and discharge process. The bigger one, with a base edge of 1 μm and a thickness of 0.25 μm, was twice as the size of the small one. By changing the position state of the Zn sheets, the electric field distribution in different Zn sheet positions and stacking states can be further studied. The electrical conductivity of Zn electrode and Zn sheets was set as 1.67×10^7 S m⁻¹. The experimentally determined voltage hysteresis were employed as the cathodic potentials: the model (bare Zn) was 48 mV, while the model (NOC@Zn) was 22 mV. The anodic potential was fixed as a constant of zero.

Data availability

The data supporting the findings of this work are available within the article and its Supplementary Information files. All other relevant data supporting the findings of this study are available from the corresponding author on request.

Declarations

Acknowledgment

This work was supported by the National Key R&D Program of China (2019YFA0708201, 2019YFA0708204), National Natural Science Foundation of China (22179089, T2188101, 11904244), Science Fund for Distinguished Young Scholars of Jiangsu Province (BK20211503) and Suzhou Science and Technology Project-Pro prospective Application Research Program (SYG202038). The authors also acknowledge support from the Suzhou Key Laboratory for Advanced Carbon Materials and Wearable Energy Technologies, Suzhou, China.

Author contributions

J.S. designed the concept. X.Y. and J.L. prepared and characterized the NOC@Zn anode and KVOH cathode. X.Y., J.L., Z.S., Z.C., X.L., W.L., Y.Z., and Y.Z. performed the electrochemical test and explored the protective mechanism. C.C. conducted the DFT calculation. J.P. performed the COMSOL simulations. X.Y., J.L., M.R., S.D. and J.S. co-wrote the manuscript. All authors discussed the experimental and theoretical results and commented on the manuscript. All authors have approved to the final version of the manuscript.

Competing interests

The authors declare no competing interests.

References

1. D. Han *et al.*, A non-flammable hydrous organic electrolyte for sustainable zinc batteries. *Nat. Sustain.* DOI: 10.1038/s41893-021-00800-9, (2022).
2. J. Zheng, L. A. Archer, Controlling electrochemical growth of metallic zinc electrodes: Toward affordable rechargeable energy storage systems. *Sci. Adv.* **7**, eabe0219 (2021).
3. P. Ruan, S. Liang, B. Lu, H. J. Fan, J. Zhou, Design strategies for high-energy-density aqueous zinc batteries. *Angew. Chem. Int. Ed.* DOI: 10.1002/anie.202200598, (2022).
4. X. Yang *et al.*, Interfacial manipulation via in situ grown ZnSe cultivator toward highly reversible Zn metal anodes. *Adv. Mater.* **33**, 2105951 (2021).
5. Y. Su, X. Yang, Q. Zhang, J. Sun, Z. Liu, Carbon nanomaterials for highly stable Zn anode: Recent progress and future outlook. *J. Electroanal. Chem.* **904**, 115883 (2022).
6. B. Tang, L. Shan, S. Liang, J. Zhou, Issues and opportunities facing aqueous zinc-ion batteries. *Energy Environ. Sci.* **12**, 3288–3304 (2019).
7. C. Li, X. Xie, S. Liang, J. Zhou, Issues and future perspective on zinc metal anode for rechargeable aqueous zinc-ion batteries. *Energy Environ. Mater.* **3**, 146–159 (2020).
8. C. Li *et al.*, Directly grown vertical graphene carpets as janus separators toward stabilized Zn metal anodes. *Adv. Mater.* **32**, 2003425 (2020).
9. P. Cao *et al.*, Fast-charging and ultrahigh-capacity zinc metal anode for high-performance aqueous zinc-ion batteries. *Adv. Funct. Mater.* **31**, 2100398 (2021).

10. Z. Zhao *et al.*, Long-life and deeply rechargeable aqueous Zn anodes enabled by a multifunctional brightener-inspired interphase. *Energy Environ. Sci.* **12**, 1938–1949 (2019).
11. Z. Cai *et al.*, A replacement reaction enabled interdigitated metal/solid electrolyte architecture for battery cycling at 20 mA cm⁻² and 20 mAh cm⁻². *J. Am. Chem. Soc.* **143**, 3143–3152 (2021).
12. L. Yuan *et al.*, Regulation methods for the Zn/electrolyte interphase and the effectiveness evaluation in aqueous Zn-ion batteries. *Energy Environ. Sci.* **14**, 5669–5689 (2021).
13. J. Zheng *et al.*, Surface and interface engineering of Zn anodes in aqueous rechargeable Zn-ion batteries. Small DOI: 10.1002/sml.202200006, (2022).
14. J. Zhou *et al.*, Ultrathin surface coating of nitrogen-doped graphene enables stable zinc anodes for aqueous zinc-ion batteries. *Adv. Mater.* **33**, 2101649 (2021).
15. A. Xia, X. Pu, Y. Tao, H. Liu, Y. Wang, Graphene oxide spontaneous reduction and self-assembly on the zinc metal surface enabling a dendrite-free anode for long-life zinc rechargeable aqueous batteries. *Appl. Surf. Sci.* **481**, 852–859 (2019).
16. Q. Yang *et al.*, Hydrogen-substituted graphdiyne ion tunnels directing concentration redistribution for commercial-grade dendrite-free zinc anodes. *Adv. Mater.* **32**, 2001755 (2020).
17. R. Yuksel, O. Buyukcakir, W. K. Seong, R. S. Ruoff, Metal-organic framework integrated anodes for aqueous zinc-ion batteries. *Adv. Energy Mater.* **10**, 1904215 (2020).
18. M. Zhou *et al.*, Surface-preferred crystal plane for a stable and reversible zinc anode. *Adv. Mater.* **33**, 2100187 (2021).
19. J. Zheng *et al.*, Textured electrodes: Manipulating built-in crystallographic heterogeneity of metal electrodes via severe plastic deformation. *Adv. Mater.* **34**, 2106867 (2022).
20. X. Yang *et al.*, In situ separator modification via CVD-derived N-doped carbon for highly reversible Zn metal anodes. *Nano Res.* DOI: 10.1007/s12274-021-3957-z, (2022).
21. B. Liu *et al.*, Oxygen-assisted direct growth of large-domain and high-quality graphene on glass targeting advanced optical filter applications. *Nano Res.* **14**, 260–267 (2021).
22. W. Guo *et al.*, Oxidative-etching-assisted synthesis of centimeter-sized single-crystalline graphene. *Adv. Mater.* **28**, 3152–3158 (2016).
23. Z. Xu *et al.*, Efficient Zn metal anode enabled by O,N-codoped carbon microflowers. *Nano Lett.* **22**, 1350–1357 (2022).
24. C. Lu *et al.*, Enhanced kinetics harvested in heteroatom dual-doped graphitic hollow architectures toward high rate printable potassium-ion batteries. *Adv. Energy Mater.* **10**, 2001161 (2020).
25. J. Shan *et al.*, Ethanol-precursor-mediated growth and thermochromic applications of highly conductive vertically oriented graphene on soda-lime glass. *ACS Appl. Mater. Interfaces* **12**, 11972–11978 (2020).
26. Y. Xu *et al.*, Highly nitrogen doped carbon nanofibers with superior rate capability and cyclability for potassium ion batteries. *Nat. Commun.* **9**, 1720 (2018).

27. W. Zhang *et al.*, A site-selective doping strategy of carbon anodes with remarkable K-ion storage capacity. *Angew. Chem. Int. Ed.* **59**, 4448–4455 (2020).
28. Q. Yang *et al.*, Dendrites in Zn-based batteries. *Adv. Mater.* **32**, 2001854 (2020).
29. Y. Cui *et al.*, An interface-bridged organic-inorganic layer that suppresses dendrite formation and side reactions for ultra-long-life aqueous zinc metal anodes. *Angew. Chem. Int. Ed.* **59**, 16594–16601 (2020).
30. J. Evans, C. A. Vincent, P. G. Bruce, Electrochemical measurement of transference numbers in polymer electrolytes. *Polymer* **28**, 2324–2328 (1987).
31. S. Li *et al.*, Toward planar and dendrite-free Zn electrodepositions by regulating Sn-crystal textured surface. *Adv. Mater.* **33**, 2005424 (2021).
32. J. Zheng *et al.*, Reversible epitaxial electrodeposition of metals in battery anodes. *Science* **366**, 645–648 (2019).
33. J. Hao *et al.*, Boosting zinc electrode reversibility in aqueous electrolytes by using low-cost antisolvents. *Angew. Chem. Int. Ed.* **60**, 7366–7375 (2021).
34. F. Wang *et al.*, Highly reversible zinc metal anode for aqueous batteries. *Nat. Mater.* **17**, 543–549 (2018).
35. Q. Yang *et al.*, Stabilizing interface pH by N-modified graphdiyne for dendrite-free and high-rate aqueous Zn-ion batteries. *Angew. Chem. Int. Ed.* **61**, e202112304 (2022).
36. X. Xie *et al.*, Manipulating the ion-transfer kinetics and interface stability for high-performance zinc metal anodes. *Energy Environ. Sci.* **13**, 503–510 (2020).
37. M. Tian *et al.*, Structural engineering of hydrated vanadium oxide cathode by K⁺ incorporation for high-capacity and long-cycling aqueous zinc ion batteries. *Energy Storage Mater.* **29**, 9–16 (2020).
38. H. Lu *et al.*, Vertical crystal plane matching between AgZn₃ (002) and Zn (002) achieving a dendrite-free zinc anode. *Small* DOI: 10.1002/sml.202200131, (2022).
39. H. He, H. Tong, X. Song, X. Song, J. Liu, Highly stable Zn metal anodes enabled by atomic layer deposited Al₂O₃ coating for aqueous zinc-ion batteries. *J. Mater. Chem. A* **8**, 7836–7846 (2020).
40. R. Zhao *et al.*, Redirected Zn electrodeposition by an anti-corrosion elastic constraint for highly reversible Zn anodes. *Adv. Funct. Mater.* **31**, 2001867 (2021).
41. K. Leng *et al.*, A safe polyzwitterionic hydrogel electrolyte for long-life quasi-solid state zinc metal batteries. *Adv. Funct. Mater.* **30**, 2001317 (2020).
42. H. Yang *et al.*, A metal-organic framework as a multifunctional ionic sieve membrane for long-life aqueous zinc-iodide batteries. *Adv. Mater.* **32**, 2004240 (2020).
43. Z. Wang *et al.*, A metal-organic framework host for highly reversible dendrite-free zinc metal anodes. *Joule* **3**, 1289–1300 (2019).
44. Y. Chu *et al.*, In situ built interphase with high interface energy and fast kinetics for high performance Zn metal anodes. *Energy Environ. Sci.* **14**, 3609–3620 (2021).

45. Y. Wu *et al.*, Electrochemically derived graphene-like carbon film as a superb substrate for high-performance aqueous Zn-ion batteries. *Adv. Funct. Mater.* **30**, 1907120 (2020).
46. K. Zhao *et al.*, Ultrathin surface coating enables stabilized zinc metal anode. *Adv. Mater. Interfaces* **5**, 1800848 (2018).
47. Y. Shao *et al.*, Regulating interfacial ion migration via wool keratin mediated biogel electrolyte toward robust flexible Zn-ion batteries. *Small* **18**, 2107163 (2022).
48. X. Yang *et al.*, Ambipolar two-dimensional bismuth nanostructures in junction with bismuth oxychloride. *Nano Res.* **14**, 1103–1109 (2021).
49. G. Kresse, J. Hafner, Ab initio molecular dynamics for liquid metals. *Phys. Rev. B* **47**, 558–561 (1993).
50. G. Kresse, J. Hafner, Ab initio molecular-dynamics simulation of the liquid-metal–amorphous-semiconductor transition in germanium. *Phys. Rev. B* **49**, 14251–14269 (1994).
51. G. Kresse, J. Furthmuller, Efficient iterative schemes for ab initio total-energy calculations using a plane-wave basis set. *Phys. Rev. B* **54**, 11169–11186 (1996).
52. P. E. Blochl, Projector augmented-wave method. *Phys. Rev. B* **50**, 17953–17979 (1994).
53. J. P. Perdew, K. Burke, M. Ernzerhof, Generalized gradient approximation made simple. *Phys. Rev. Lett.* **77**, 3865–3868 (1996).
54. H. J. Monkhorst, J. D. Pack, Special points for Brillouin-zone integrations. *Phys. Rev. B* **13**, 5188–5192 (1976).
55. S. Grimme, J. Antony, S. Ehrlich, H. Krieg, A consistent and accurate ab initio parametrization of density functional dispersion correction (DFT-D) for the 94 elements H-Pu. *J. Chem. Phys.* **132**, 154104 (2010).
56. X. Zhang *et al.*, Ultra-long-life and highly reversible Zn metal anodes enabled by a desolvation and deanionization interface layer. *Energy Environ. Sci.* **14**, 3120–3129 (2021).
57. J. Shin *et al.*, Highly reversible, grain-directed zinc deposition in aqueous zinc ion batteries. *Adv. Energy Mater.* **11**, 2100676 (2021).
58. Z. Zhao *et al.*, Horizontally arranged zinc platelet electrodeposits modulated by fluorinated covalent organic framework film for high-rate and durable aqueous zinc ion batteries. *Nat. Commun.* **12**, 6606 (2021).
59. L. Hong *et al.*, Toward hydrogen-free and dendrite-free aqueous zinc batteries: Formation of zincophilic protective layer on Zn anodes. *Adv. Sci.* **9**, 2104866 (2022).
60. L. Kang *et al.*, Nanoporous CaCO₃ coatings enabled uniform Zn stripping/plating for long-life zinc rechargeable aqueous batteries. *Adv. Energy Mater.* **8**, 1801090 (2018).
61. Q. Zhang *et al.*, Revealing the role of crystal orientation of protective layers for stable zinc anode. *Nat. Commun.* **11**, 3961 (2020).
62. J. Hao *et al.*, An in-depth study of Zn metal surface chemistry for advanced aqueous Zn-ion batteries. *Adv. Mater.* **32**, 2003021 (2020).

63. C. Deng *et al.*, A sieve-functional and uniform-porous kaolin layer toward stable zinc metal anode. *Adv. Funct. Mater.* **30**, 2000599 (2020).
64. D. Han *et al.*, A corrosion-resistant and dendrite-free zinc metal anode in aqueous systems. *Small* **16**, 2001736 (2020).
65. Z. Cao *et al.*, Eliminating Zn dendrites by commercial cyanoacrylate adhesive for zinc ion battery. *Energy Storage Mater.* **36**, 132–138 (2021).
66. Y. Zhou *et al.*, 3D confined zinc plating/stripping with high discharge depth and excellent high-rate reversibility. *J. Mater. Chem. A* **8**, 11719–11727 (2020).
67. Y. Zeng *et al.*, Dendrite-free zinc deposition induced by multifunctional CNT frameworks for stable flexible Zn-ion batteries. *Adv. Mater.* **31**, 1903675 (2019).
68. J. Cao *et al.*, A universal and facile approach to suppress dendrite formation for a Zn and Li metal anode. *J. Mater. Chem. A* **8**, 9331–9344 (2020).

Figures

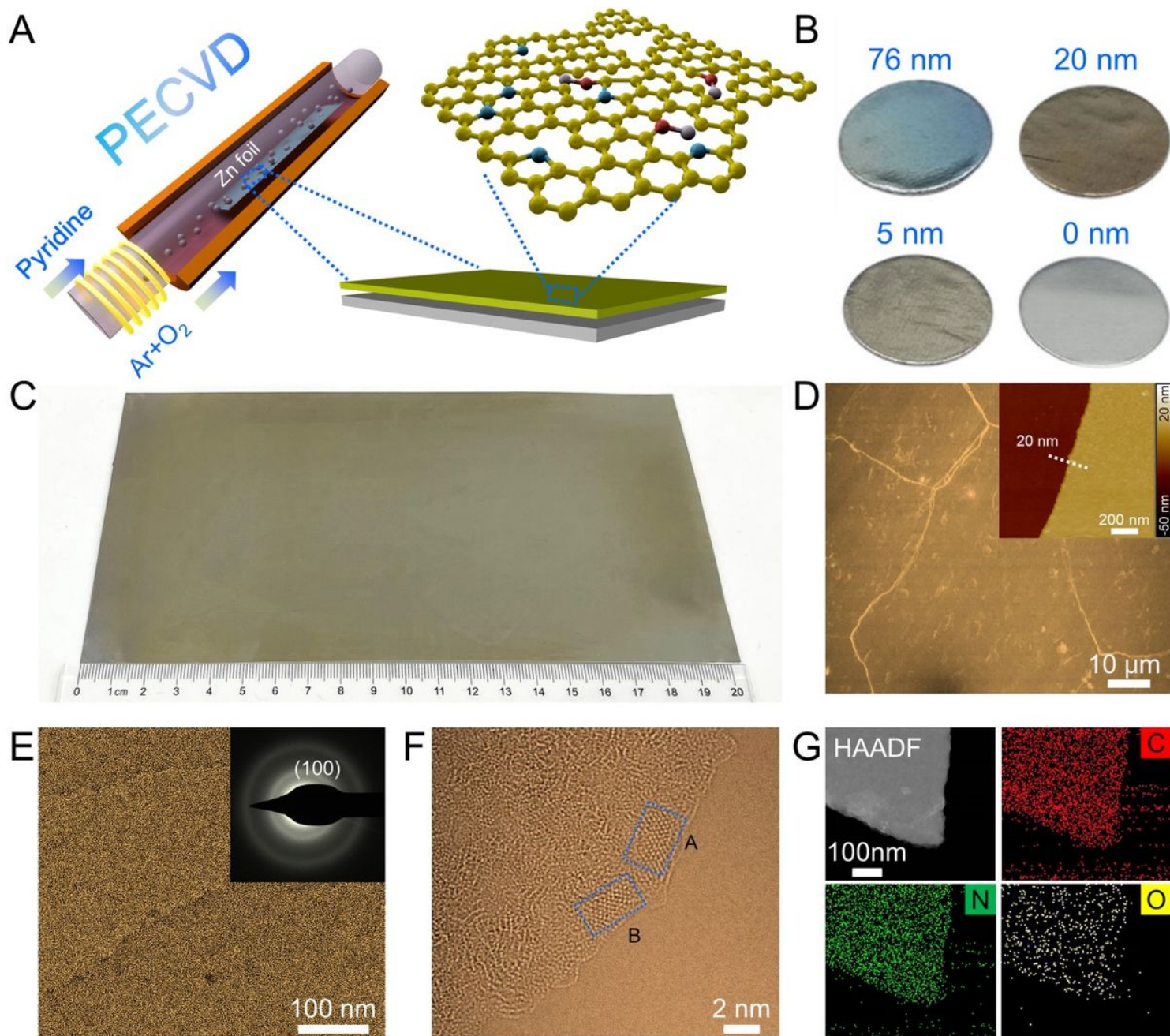


Figure 1

Synthesis and characterization of NOC@Zn. (A) Schematic illustration of the PECVD growth of uniform NOC overlayer on Zn foil. (B) Photograph of NOC@Zn with different NOC thicknesses. (C) Photograph showing a NOC@Zn foil grown in 4-inch quartz tube. (D) Top-view SEM image of NOC@Zn. Inset: AFM image of NOC overlayer. (E) TEM image of NOC overlayer. Inset: the corresponding SAED pattern. (F) HRTEM image of NOC overlayer. (G) EDS mapping of NOC overlayer.

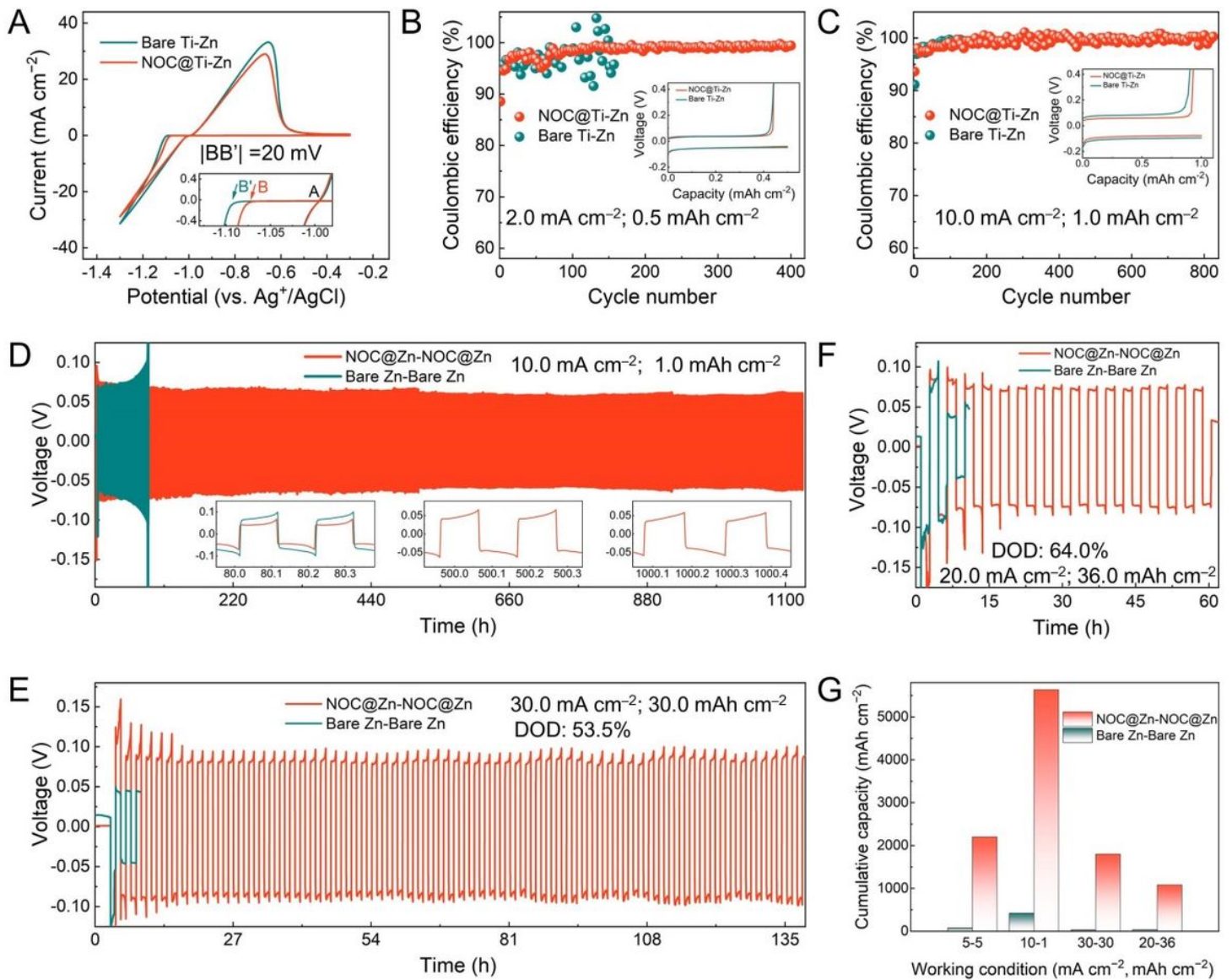


Figure 2

Electrochemical performances of NOC@Zn anode. (A) CV curves for NOC@Ti-Zn and bare Ti-Zn cells at a scan rate of 1 mV s^{-1} . CE measurement of NOC@Ti-Zn and bare Ti-Zn cells under (B) $2.0 \text{ mA cm}^{-2}/0.5 \text{ mAh cm}^{-2}$ and (C) $10.0 \text{ mA cm}^{-2}/1.0 \text{ mAh cm}^{-2}$. Inset: Corresponding voltage-capacity profiles of the first cycle. Cycling performances of symmetric cells at (D) $10.0 \text{ mA cm}^{-2}/1.0 \text{ mAh cm}^{-2}$, (E) $30.0 \text{ mA cm}^{-2}/30.0 \text{ mAh cm}^{-2}$, and (F) $20.0 \text{ mA cm}^{-2}/36.0 \text{ mAh cm}^{-2}$. (G) Cumulative capacity of NOC@Zn and bare Zn anodes at various working conditions.

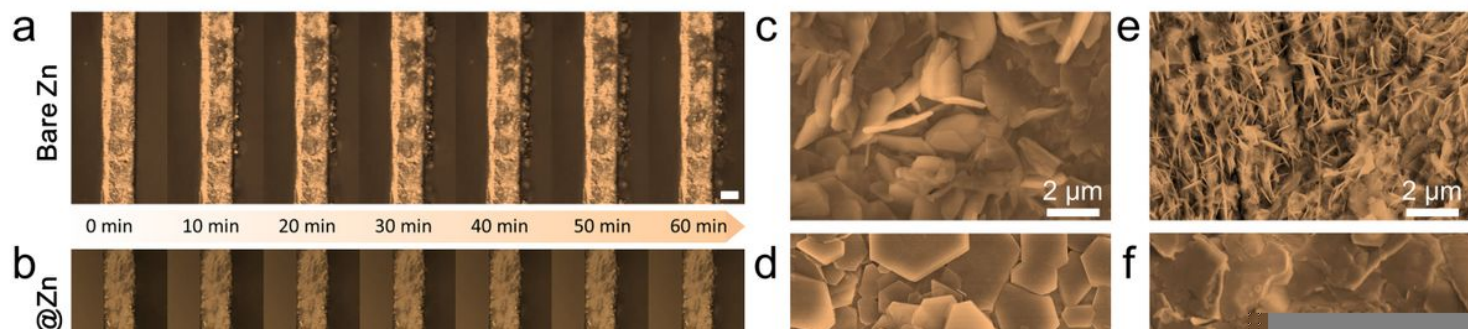


Figure 3

Instrumental insights into the protective effect of NOC overlayer. *Operando* optical microscopy visualization of Zn plating on (A) bare Zn and (B) NOC@Zn electrode at 5.0 mA cm^{-2} . Scale bars: $50 \mu\text{m}$. Top-view SEM images of (C) bare Zn and (D) NOC@Zn electrodes after plating of 1.0 mAh cm^{-2} with a current density of 10.0 mA cm^{-2} . Top-view SEM images of (E) bare Zn and (F) NOC@Zn electrodes after 100 cycles under $10.0 \text{ mA cm}^{-2}/1.0 \text{ mAh cm}^{-2}$. Optical surface profilometry images of (G) bare Zn and (H) NOC@Zn after 100 cycles under $10.0 \text{ mA cm}^{-2}/1.0 \text{ mAh cm}^{-2}$. (I) XRD patterns of bare Zn and NOC@Zn electrodes after 100 cycles under $10.0 \text{ mA cm}^{-2}/1.0 \text{ mAh cm}^{-2}$. (J) Nyquist plots of NOC@Zn symmetric cell before and after polarization. Inset: Current evolution of NOC@Zn symmetric cell under polarization of 10 mV. Simulated electric field distributions on (K) bare Zn and (L) NOC@Zn electrodes.

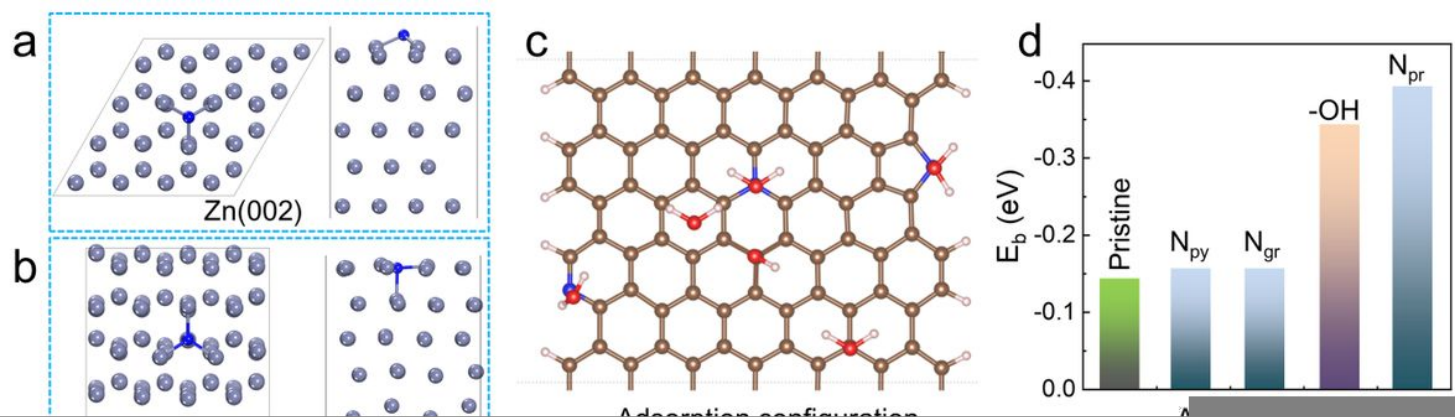


Figure 4

Theoretical calculation and electrochemical analysis. Optimized adsorption models of N atom on (A) Zn (002) and (B) Zn (100) planes. The gray and blue balls denote the zinc and nitrogen atoms, respectively. (C) The adsorption configuration of water molecule on NOC layer. The brown, red, blue, and white balls indicate carbon, oxygen, nitrogen, and hydrogen atom, respectively. (D) The binding energy of water molecule on different adsorption sites. (E) Nyquist plots at different temperatures for NOC@Zn. (F) Arrhenius curves and comparison of activation energies of bare Zn and NOC@Zn. (G) Linear polarization curves presenting the corrosion on bare Zn and NOC@Zn. Schematic diagram of (H) bare Zn and (I) NOC@Zn electrodes upon electrochemical cycling.

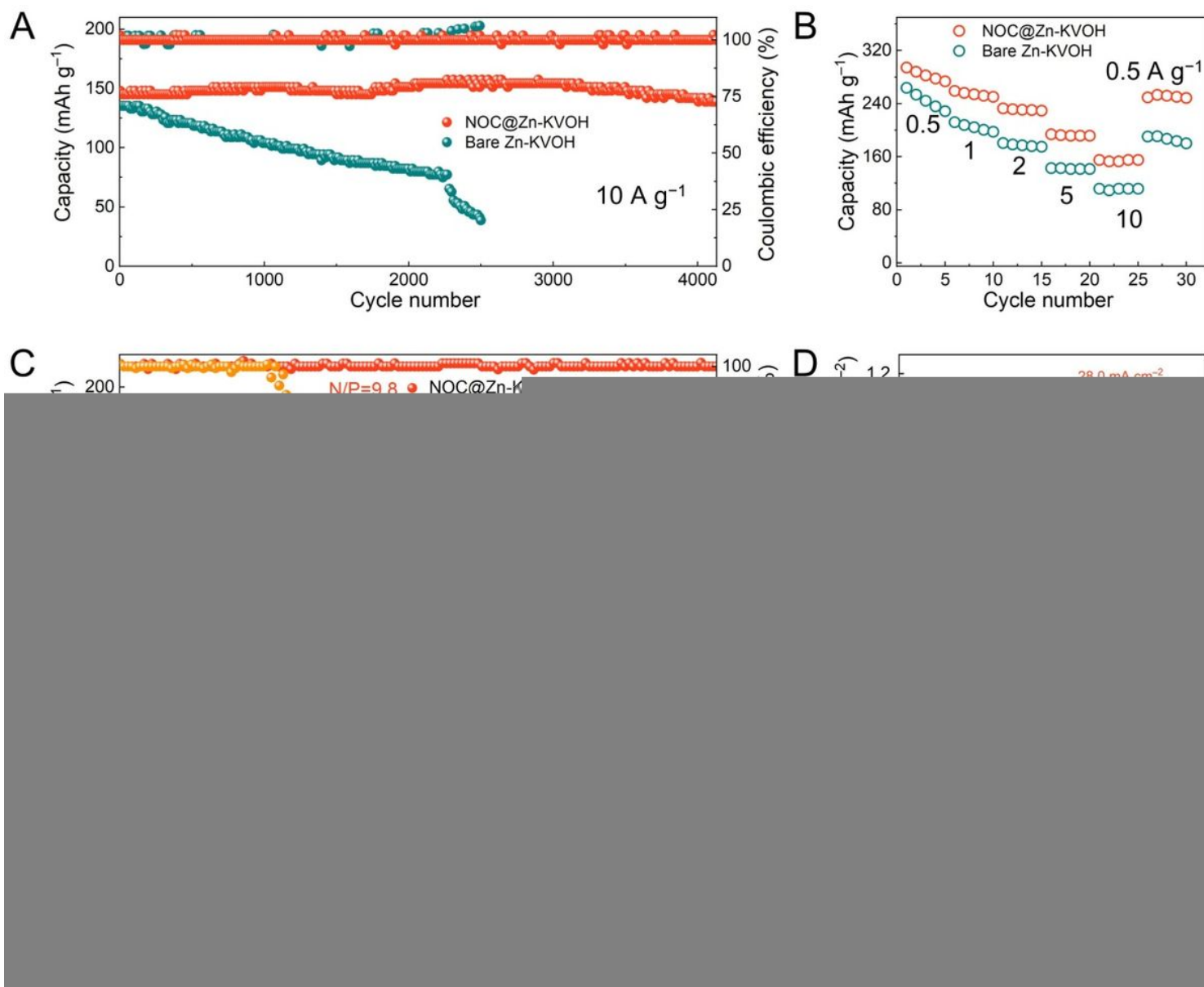


Figure 5

Electrochemical performances of Zn-ion full cells. (A) Cycling performance at 10.0 A g^{-1} for 4000 cycles. (B) Rate performance. (C) Cycling performance at N/P ratio of 9.8 and 3.5. (D) Comparison of current density and areal capacity between this work and previous reports. (E) Schematic illustration of the flexible transparent battery. Digital photos showing the working states of flexible NOC@Zn-KVOH cells in series to power (F) a LED indicator and (G) a timer. (H) Cycling performance of the flexible AZIB under different bending angles. Insets: Diagrams of flexible batteries under three bending angles.

Supplementary Files

This is a list of supplementary files associated with this preprint. Click to download.

- [Sl.docx](#)